

A one-year seasonal analysis of Martian gravity waves using MCS Data

Corwin Wright^{a,b}

^aLaboratoire de Physique des Océans, Université de Bretagne Occidentale, Brest, Finistère 29200, France

^bAtmospheric Chemistry Division, National Center for Atmospheric Research, Boulder, Colorado 80301, USA

Abstract

Temperature measurements from the Mars Climate Sounder on NASA's Mars Reconnaissance Orbiter are examined for gravity wave signals using the Stockwell Transform, a technique previously applied to terrestrial temperature profiles. An analysis is presented for internal-gravity waves throughout the Martian atmosphere for the period July 2007 to May 2009, representing a full Martian year of data, divided by season. Momentum fluxes observed in the altitude range 200 Pa – 20 Pa are measured as $\sim 10^{-5}$ – 10^{-3} Pa, significantly higher than at equivalent altitudes on Earth, and are primarily peaked around the tropics. Observed orographic effects are minimal; the primary observed effects are seasonal. Waves are shown to vary significantly in wavelength with latitude, but are generally approximately zonally symmetric. Horizontal wavelengths are consistently much shorter in the northern hemisphere than the southern.

Keywords: Atmospheres, dynamics, Mars, atmosphere, Infrared observations

1. Introduction

Gravity waves are a type of wave process in which fluid pressure, temperature, density and velocity fluctuate together, and arise in fluids via the interaction between gravity and buoyancy. In atmospheres, such waves exist across a wide range of length scales, from small acoustic-gravity waves on scales of tens of metres in the horizontal and vertical to planetary-scale Rossby waves with wavelengths comparable to the circumference of the planet [Andrews, 2000].

Gravity waves make a major contribution to the dynamics and structure of atmospheres at all scales, providing a significant mechanism whereby momentum can be transferred between different regions without corresponding mass transfer. In a fluid with no significant upper boundary such as a planetary atmosphere, such waves can propagate vertically through most of the available height range. Such propagating waves carry a vertical flux of horizontal momentum (hereafter a 'momentum flux'), with the momentum deposited from their breaking, dissipation and absorption providing a major source of forcing at higher altitudes [Fritts and Alexander, 2003].

Gravity waves in the Martian atmosphere have been observed in many studies and with a variety of methods, from lee waves observed in cloud by Mariner 9 in the mid-1970s [Briggs and Leovy, 1974, Pirraglia, 1976]

to lander accelerometer [Magalhães *et al.*, 1999], satellite aerobraking [Fritts *et al.*, 2006] and radio occultation [Creasey *et al.*, 2006] techniques in the 1990s and 2000s. Evidence has been seen of significant dynamical alterations at high altitudes due to the momentum transported by the propagation of these waves, including enhanced diffusion, mean temperatures far above radiative equilibrium at winter polar latitudes, and zonal jet closure. Modelling studies [e.g. Barnes, 1990, Joshi *et al.*, 1995, Collins *et al.*, 1997, Angelats i Coll *et al.*, 2005] have also shown the importance of gravity waves to Martian atmospheric structure. To date, however, the limited resolution of measurements of the Martian atmosphere has made it difficult to measure this driving. The newest generation of instruments, however, provides the opportunity to measure portions of the wave spectrum directly.

2. The Mars Climate Sounder

The Mars Climate Sounder (MCS) is a nine-channel passive radiometer aboard NASA's Mars Reconnaissance Orbiter spacecraft, currently in a polar sun-synchronous orbit around Mars [McCleese *et al.*, 2007]. Designed to measure horizontally-contiguous radiance profiles from the atmospheric limb and nadir from the surface to an altitude of 80 km, MCS began taking measurements in September 2006 [Kleinböhl *et al.*,

2009]. Due to a mechanical anomaly, the instrument was placed into a limb-staring mode from February 2007 until June 2007, at which point limb-scanning resumed. More than a full Martian year of data have now been obtained.

The temperature data used are the Level 2 product described by Kleinböhl *et al.* [2009], obtained from the Planetary Data System (PDS). This provides vertical temperature profiles over the range 5–10 km to 80–90 km, with a vertical resolution of 4–6 km and with a temperature precision of between 0.5–2 K over this range, retrieved via a fast radiative transfer scheme using the infrared channels of the instrument.

In this study, we examine data from the 13th of October 2007 to the 29th of August 2009. This represents a full Martian year (687 days, 667 Sols) of data, and is slightly offset from the Martian seasonal cycle, starting 58 days before the 2007 vernal equinox and ending 58 days before the 2009 vernal equinox. This is due to data availability: before the beginning date, only an extremely limited number of profiles were retrieved at most latitudes due to an extended dust storm covering almost the whole planet, and after the end date, the instrument was switched off for a period of several months. Accordingly, in the seasonal analyses outlined below, data from winter 2007 have been combined with data from winter 2009 in order to provide a full season for analysis. This has obvious limitations in that, while seasonal effects may average appropriately, effects which are different between the two separate winters may cancel out slightly; accordingly, time series will also be shown to disambiguate such effects as far as possible. Table 1 describes the precise dates used, together with the solar longitude L_S associated with the start and end of each season, and the number of elapsed Sols this corresponds to. References to seasons in this study should be taken to describe seasonality in the northern hemisphere unless specified.

3. Wave Detection Algorithm

The method used to analyse the MCS temperature profiles is that outlined by Alexander *et al.* [2008]. This method has previously been used to examine terrestrial temperature profiles for gravity wave signals in a range of studies [e.g. Stockwell and Lowe, 2000, Wang *et al.*, 2006].

Initially, daily vertical temperature profiles are binned onto a 6° latitude \times 40° longitude array, with each height level treated independently. Any gaps in the data are then interpolated over in the longitudinal direction, and planetary-scale oscillations (zonal mean and

wavenumbers 1–3) are computed using a Fourier transform. These values are then interpolated onto the scan track of the satellite measurements, and removed from the individual temperature measurements to leave profiles of localised temperature perturbations.

The Stockwell (S-) Transform [Stockwell *et al.*, 1996] is then applied to the perturbation profiles. This provides a height-frequency representation of the spectral signals present in the perturbation profile as a complex-valued function of height and frequency $\tilde{T}(z, k_z)$. For each adjacent profile-pair ($i, i + 1$) the cospectrum

$$C_{i,i+1} = \tilde{T}_i \tilde{T}_{i+1}^* \quad (1)$$

and covariance spectrum $|C_{i,i+1}|$ are then computed.

We then remove frequencies corresponding to vertical wavelengths greater than 10 km. This serves to remove the effect of thermal tides, which dominate the Martian tropical atmosphere at large vertical scales [Creasey *et al.*, 2006]. We also discard any profiles where the horizontal (great-circle) separation between the measurements is greater than 120 km, in order to provide good estimates of the horizontal wavelengths detected. Next, we locate the maximum in the covariance spectrum independently for each height level. This gives us the vertical frequency m , and hence vertical wavelength $\lambda_z = 2\pi/m$, of the greatest-amplitude signal present in the profile-pair as a function of height level. We also compute the covarying temperature perturbations, i.e. wave amplitude,

$$\hat{T}_{i,i+1} = \sqrt{|C_{i,i+1}|}. \quad (2)$$

and phase difference between profiles

$$\Delta\phi_{i,i+1} = \arctan\left(\frac{\text{Im}(C_{i,i+1})}{\text{Re}(C_{i,i+1})}\right). \quad (3)$$

From this phase difference, we compute the horizontal wavenumber of the signal along the horizontal path between the two profiles via the relationship

$$k_h = \frac{\Delta\phi_{i,i+1}}{\Delta r_{i,i+1}}, \quad (4)$$

where $\Delta r_{i,i+1}$ represents the great-circle distance between the two profiles at that height level. It should be noted that, as the horizontal wavevector of the internal wave is unlikely to lie directly along the direction of travel of the instrument, horizontal wavenumbers are accordingly likely to be significantly underestimated. Therefore, k_h is likely to be an underestimate [see e.g. Ern *et al.*, 2004], as it represents only the component of the wave lying in the direction between the measurements.

Table 1: Seasons

Season	Dates	Days	L_S	Sols
Winter (1)	2007/10/13 — 2007/12/09	58	330 — 360	55
Spring	2007/12/10 — 2008/06/24	198	0 — 90	192
Summer	2008/06/25 — 2008/12/24	183	90 — 180	177
Autumn	2008/12/25 — 2009/05/20	147	180 — 270	143
Winter (2)	2009/05/21 — 2009/08/29	101	270 — 330	97

After this step, we now have the magnitude, vertical wavelength, and horizontal wavenumber of the signal, and can accordingly use the relationship

$$M_{i,i+1} = \frac{\rho}{2} \lambda_z \frac{k_h}{2\pi} \left(\frac{g}{N}\right)^2 \left(\frac{\hat{T}_{i,i+1}}{\bar{T}}\right)^2, \quad (5)$$

to compute the magnitude of the vertical flux of horizontal momentum ('momentum flux', $M_{i,i+1}$) of the projection of the wave along the line connecting the two points, where ρ is the background atmospheric density, g the acceleration due to Mar's gravity, N the Brunt-Väisälä frequency, and \bar{T} the unperturbed background temperature [Ern *et al.*, 2004].

In this calculation, we approximate the Brunt-Väisälä frequency to $N = 0.008 \text{ rad s}^{-1}$ [Imamura and Kobayashi, 2009], and the atmospheric density to the simplified relation

$$\rho = \rho_0 \exp(-z/H) \quad (6)$$

for Martian surface atmospheric density $\rho_0 = 1.89 \times 10^{-2} \text{ kg m}^{-3}$ and scale height $H = 11.1 \text{ km}$. The background temperature \bar{T} is taken from a mean over the box defined as five height levels above and below and five profiles before and after the measurement under consideration.

This calculation assumes that the internal waves can be considered to be within the midfrequency regime $N \gg \hat{\omega} \gg f$, where $\hat{\omega}$ is the wave intrinsic frequency

$$\hat{\omega}^2 = \frac{N^2(k^2 + l^2) + f^2(m^2 + \frac{1}{4H^2})}{k^2 + l^2 + m^2 + \frac{1}{4H^2}}, \quad (7)$$

f the Coriolis parameter $f = 2\Omega \sin(\Phi)$, Ω the planetary rotation frequency, Φ the latitude under consideration, and k and l the horizontal wavenumber of the wave in the longitudinal and latitudinal directions respectively. For the sampling frequencies of MCS at horizontal and vertical wavelengths of the order of hundreds of kilometres and of the order of ten kilometres respectively, this relationship is true.

Due to the lack of two-dimensional data at any given height level and the instantaneous sampling of

the waves, the results obtained for momentum flux do not possess directional information [Alexander *et al.*, 2008]; that is to say that the results represent a magnitude rather than a vector quantity. Also, waves with a horizontal wavelength along the scan track of shorter than the Nyquist sampling limit, $\sim 200 \text{ km}$, do not contribute directly to the measured momentum flux due to the distance between profiles, but can be aliased, leading to them being measured with the wrong wavelength. The measurements may be sensitive to, but undersample, waves with short horizontal wavelengths, and, consequently, may contribute to the signal with an underestimated momentum flux [Alexander *et al.*, 2008]. Vertical wavelengths of less than twice the vertical resolution, approximately 4–6 km, are not Nyquist sampled in the original data but instead calculated from the interpolated level 2 data, and consequently cannot be measured; accordingly, regions with vertical wavelengths $\leq 8 \text{ km}$, the upper bound of resolution, are shown in greyscale on our plots. It should be borne in mind when considering these results, however, that even the regions shown in colour may be undersampled in many profiles.

4. Data Coverage

Figure 1 shows the number of profiles analysed after filtering as a zonal mean plotted against latitude and solar longitude (after figure 23 of Kleinböhl *et al.* [2009]). As can be seen, there is a much greater coverage of results during the first half of the period considered, particularly at high southern latitudes, whilst the later portion period has limited coverage at latitudes north of around 30°S. We must thus take this into account when analysing our results; in particular, results at high southern latitudes consist of much more data than those at other latitudes, and are correspondingly more certain. Regions with no data are interpolated over in our figures where the period is less than a week, and left blank otherwise.

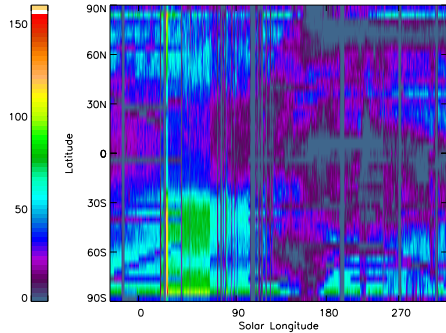


Figure 1: Coverage chart of MCS data as a function of (vertical) zonal sum latitude and (horizontal) solar longitude. Note the excellent coverage at southern latitudes in northern spring, and the poor coverage at equatorial, mid- and northern polar latitudes throughout the rest of the year.

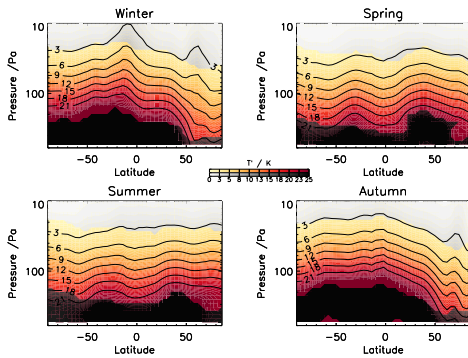


Figure 2: Temperature perturbations as a function of pressure and latitude for the four seasons considered.

5. Seasonal Zonal Means

Figures 2 – 5 show seasonal zonal means for the four properties considered in our analysis: temperature perturbations due to gravity waves (T' , figure 2), vertical wavelengths (λ_z , figure 3), horizontal wavenumbers (k_h , figure 4), and momentum fluxes (MF, figure 5). Analyses were run from the surface at 600 Pa to the 1 Pa level; at this altitude, ~ 50 km, detector noise starts to have a noticeable influence on the uncertainty of the radiance ratio used to compute the pressure scale [Kleinböhl *et al.*, 2009]. Above the 20 Pa level, however, no measured regions had vertical wavelengths in the resolved range; consequently, figures terminate at the 10 Pa level

Considering first the temperature perturbations in figure 2, we observe variations in season, height, and latitude. The most obvious characteristic is a strong decline in wave amplitude with altitude, with values in the tens of Kelvin at ~ 200 Pa falling to less than 1 K at higher altitudes. We next observe a (much smaller)

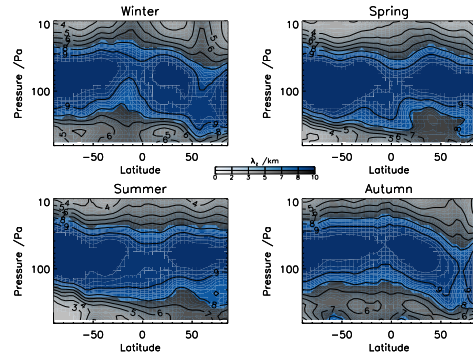


Figure 3: Vertical wavelengths as a function of pressure and latitude for the four seasons considered. The greyscale regions indicate those areas where estimated vertical wavelengths are shorter than the resolution of the instrument allows the accurate detection of.

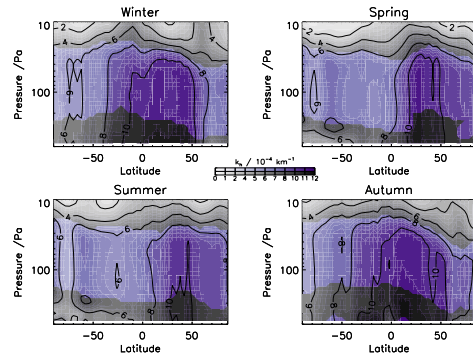


Figure 4: Horizontal wavenumbers as a function of pressure and latitude for the four seasons considered.

seasonal imbalance; amplitudes peak at >25 K in autumn and winter, whilst spring and summer values peak at ~ 20 K. There is also a geographical and latitudinal imbalance in this seasonal variation; spring and summer values peak at the lowest altitudes measured and are evenly spread in spring and slightly northwards-peaked in summer, whilst autumn and winter values peak higher up and further towards the south. Values are generally higher at all altitudes in autumn and winter.

We next examine the vertical wavelengths, figure 3. These results are generally poorly-resolved - only in the altitude band between ~ 250 Pa and ~ 20 Pa are values in the frequency range between instrument-resolved and tidal. This is true in all four seasons, but we can still draw some conclusions from the obtained results. Firstly, in all four seasons, a region of shorter vertical wavelength is observed near the equator, but this region is centred slightly south of the equator in autumn and winter and slightly north of the equator in spring and summer. This region is also broader in winter and (espe-

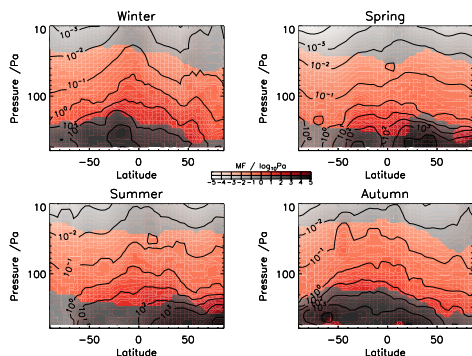


Figure 5: Momentum fluxes as a function of pressure and latitude for the four seasons considered.

cially) summer than in the other two seasons. Secondly, autumn and winter see the long-wavelength band curving downwards towards the surface towards the northern pole, with a slight rise again within 10° of the pole; while there is a definite tendrill of this region reaching towards the surface in spring and summer, the upper end of the band does not bend significantly towards the surface as well, as it does in autumn and winter.

Horizontal wavenumbers are shown in figure 4. In all four seasons, the detected waves are longer at the southern pole than the northern. In spring and summer, a region of shorter waves, $k_h \sim 10^{-3} \text{km}^{-1}$ dominates the northern hemisphere at low altitude, whilst in autumn and winter this peak shifts to northern midlatitudes and extends into the southern hemisphere.

Finally, we consider the momentum fluxes derived from these values, figure 5. The first, and most obvious observation from this figure is that MF drops exponentially with altitude; this is due primarily to the strong density and temperature dependence of the MF computation (equation 5), and is consistent with terrestrial results. Aside from this, results for MF vary little between seasons; in all four seasons the great majority of measured MF in all seasons is centred on the equator, with low values at the poles. This contrasts with the results for T' and k_h , which show significant seasonal asymmetries between the two hemispheres. MF values in spring are lower than the other three seasons at all latitudes.

6. Latitude-Time Series

We next consider time series of our variables, zonally averaged at the 100 Pa level, as shown in figure 6. At this level, vertical wavelengths $\geq 8 \text{km}$ at almost all locations and times, and consequently we have good coverage for our analyses.

We again examine first temperature perturbations (upper left). At the start of the analysis during northern winter, there is a high-amplitude (20 K) peak centred south of the equator, falling off to both the north and south but to much lower values at the north (5 K) pole than at the south (15 K). As we move into spring, this peak sharply reduces, splitting into separate peaks to the north and south of the equator. The southern peak dies away quickly, vanishing almost completely by $L_s \sim 15^\circ$, while the northern peak migrates towards the pole as spring proceeds, reaching it by the start of summer at $L_s \sim 90^\circ$. Amplitudes remain above 15 K in this migrating northern peak, rising to around 18 K as it reaches the pole. Around the same time, amplitudes at the equator reach their lowest value of the whole period analysed, around 10 K. As summer proceeds, the peak migrates southwards again, with values at the pole falling away. A peak of 18 K, stretching from 30°S to 45°N , appears rapidly in late summer, which falls away slightly but then amplifies significantly as autumn proceeds, reaching a peak of 20 K in late autumn, $L_s \sim 240^\circ$. By this time, the heightened regions extends from the southern polar region to northern midlatitudes, with the strongest signals initially centred on the equator and then in southern midlatitudes. By this time, northern polar amplitudes have fallen to below 6 K. Finally, as winter begins, values fall away slightly at all latitudes and the heightened region pulls away from the southern pole heading northwards again.

Examining next vertical wavelengths (top right), it is difficult to draw any significant conclusions: values remain at the upper cutoff of our analysis, $\sim 10 \text{km}$, for almost the entire duration of the analysis at all latitudes. There are a few exceptions. In particular, during the three periods of highest wave amplitudes, vertical wavelengths fall away rapidly, climbing again when amplitudes fall. There are also some periods of slightly reduced values at northern polar latitudes, but these are fairly small.

Horizontal wavelengths (bottom left) show minimal variation across the duration of the study, with waves generally shorter in the northern hemisphere and longer in the southern. As with temperature perturbations, there is a general drift first northwards and then southwards of the short-wavelength region southwards throughout the year, with waves lengthening slightly near the north pole during autumn and both winters. This difference could potentially be a sampling issue; as discussed above, the technique will tend to underestimate horizontal wavenumbers for waves propagating at a significant angle to the scan track of the instrument. However, given that the difference seems to apply to

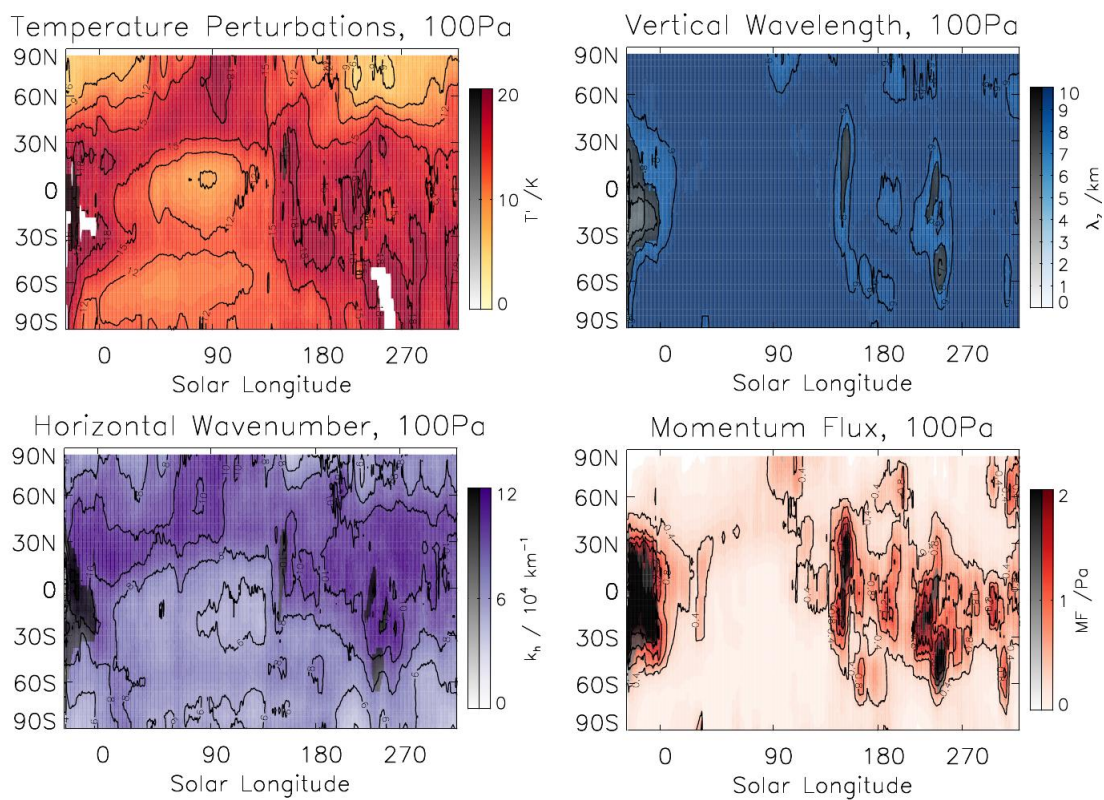


Figure 6: (top left) Temperature perturbations, (top right) vertical wavelengths, (bottom left) horizontal wavenumbers and (bottom right) momentum fluxes measured for the Martian atmosphere as a function of (horizontal) solar longitude and (vertical) latitude at the 100 Pa level

the whole hemisphere, this is unlikely: the scan track is broadly equivalent over the two hemispheres, so there would need to be a consistent difference in wave propagation directions between the hemispheres for this to be the cause of the different measured values, something which would be interesting in and of itself but which cannot be determined from these measurements.

Finally, we consider momentum flux (bottom right). Strong peaks are again observed around $L_s \sim 10^\circ$, $L_s \sim 160^\circ$ and $L_s \sim 240^\circ$, consistent with the variations in the three input variables. Results are however decoupled from temperature perturbations in some times and places, particularly in the first half of the analysed period. Here, due to the high horizontal wavenumbers observed simultaneously, the larger temperature perturbations in the northern hemisphere do not correspond strongly with waves carrying significant momentum: although the waves are high-amplitude, they are comparatively small in horizontal scale. Levels of MF observed are very ‘choppy’; throughout late summer, autumn and the second winter levels remain higher than spring and early summer at most latitudes, but are punctuated with peaks where levels rise sharply to significantly above the local mean, remain high for at most a few weeks, and then die away sharply. Combined with the results for the other variables, our results suggest that, while there is a strong seasonal component to the levels of MF measured, significant ‘flurries’ of high-amplitude high-frequency waves are often triggered, contributing large amounts of momentum to the upper atmosphere orders of magnitude above that due to seasonal variation.

7. Maps

Finally, we consider figures 7 – 10. These figures show seasonal-mean results for our four derived variables as maps at three different height levels: 100 Pa, 60 Pa and 20 Pa. These show the longitudinal as well as latitudinal distribution of the measured parameters, presenting a different perspective on the data in figures 2 – 5.

We again examine first the temperature perturbations, figure 7. In winter (top row), we observe, as seen in figure 2, that the dominant signals at all height levels are centred in a band slightly to the south of the equator, reaching peak amplitudes of 20 K at the 100 Pa level, 13 K at the 60 Pa level, and 5 K at the 20 Pa level. Amplitudes fall off outside this tropical belt, with mid-latitude values of around half the tropical value at the 100 Pa and 60 Pa levels. This tropical spike can also be clearly seen at all levels in the upper left panel of figure

2. Mean values in the northern polar region are on average lower than in the southern polar region, but with secondary peaks at around $\theta = -150$ – -90° and $\theta = 0$ – 100° at the 60 Pa level; these features produce a significant spike in the zonally-averaged T' at these latitudes, but can be clearly seen to be restricted in longitude. Values around the southern pole are broadly longitudinally symmetric at all heights.

As we move into spring, we see measured levels drop off significantly at all levels, with slightly higher values at midlatitudes than in the tropics. A pair of longitudinally-restricted peaks are seen at all levels in the northern hemisphere, one centred at $\theta = -30$ and the other at $\theta = 120$. Levels throughout the northern hemisphere are higher than in the southern hemisphere, consistent with figure 6; the seasonal averaging, however, hides the strong polar peak seen in late spring. Summer is fairly uneventful. Finally, autumn exhibits much higher levels at all locations for the lower two levels; as in winter, values are significantly higher in the southern hemisphere than the northern, and the highest values are centred slightly south of the equator at all longitudes. At the 10 Pa level, however, levels remain at slightly above their summertime levels, without the significant tropical peaks seen in winter.

Measured vertical wavelengths (figure 8), as we saw earlier, vary little with latitude - values at each level typically vary only by $\sim 10\%$ over the globe at the 100 Pa level and 60 Pa level; more variability may potentially exist at the 10 Pa, but the dominant waves at this altitude are too short to resolve properly. At both the 100 Pa and 60 Pa levels, low values are measured at the equator in all four seasons, with the exception of autumn at the 60 Pa level; this difference is also very minor at the 100 Pa level in spring. Shorter wavelengths are also measured at the 60 Pa level in the northern polar region in autumn and winter, and at the 100 Pa level in all seasons except spring. Results are largely meridionally symmetric.

Measured horizontal wavenumbers (figure 9) are almost entirely zonally symmetric; values vary by only a few percent around any given line of latitude at any level. As in figures 4 and 6, we see hemispheric and height differences. Northern hemisphere values are also typically higher than southern, with the peak shifting southwards in autumn and winter as discussed in section 5.

Finally, momentum fluxes (figure 10), as seen in section 5, are primarily peaked near the equator at all levels, falling off towards the poles. This peak is centred slightly north of the equator in spring and summer and slightly south of the equator in winter. Aside from

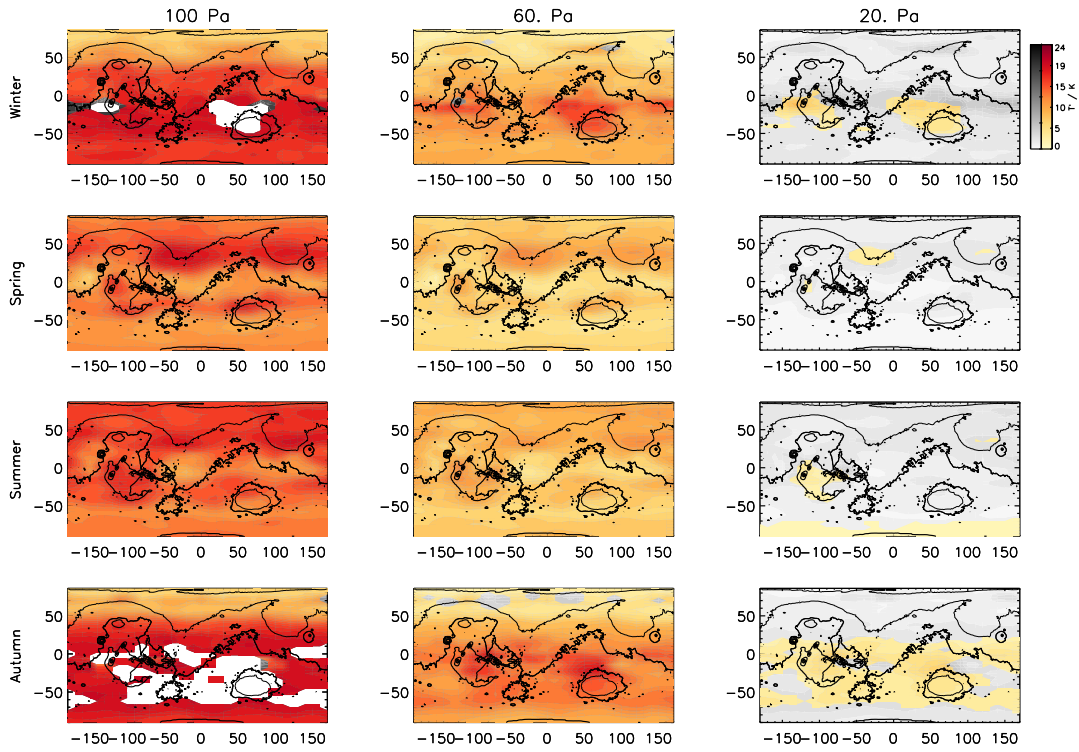


Figure 7: Seasonal mean temperature perturbations, mapped at three heights. Colour bars are different for each height level, and shown adjacent to the first season analysed at that level.

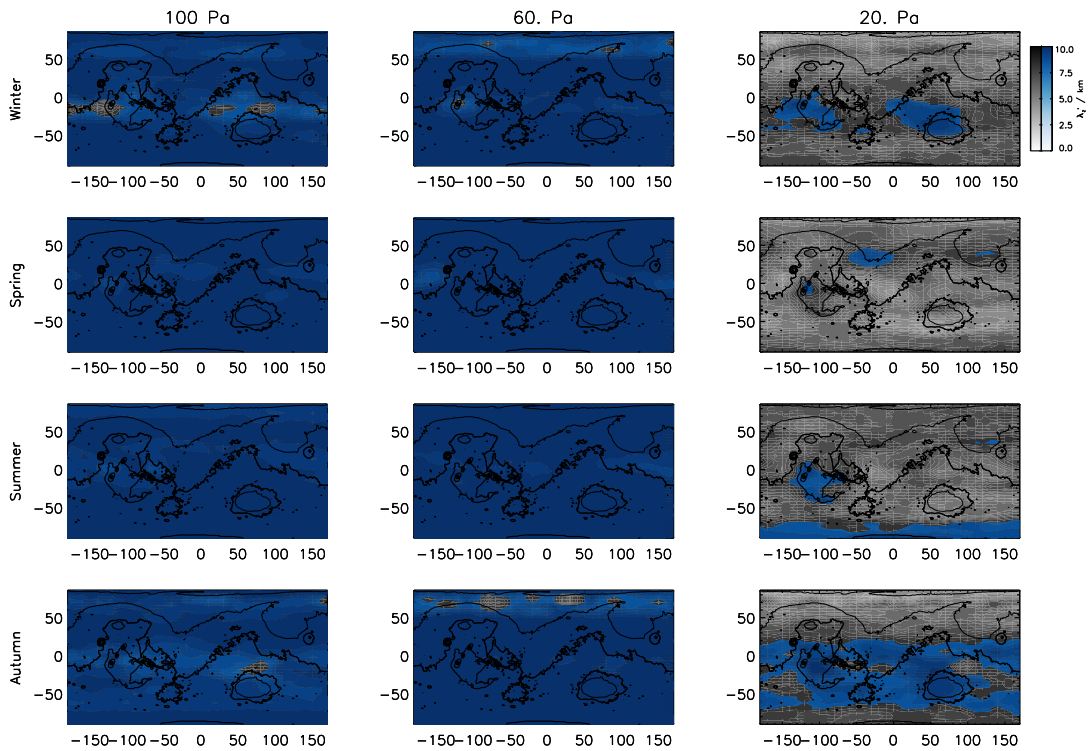


Figure 8: Seasonal mean vertical wavelengths, mapped at three heights. Colour bar for all figures at top right.

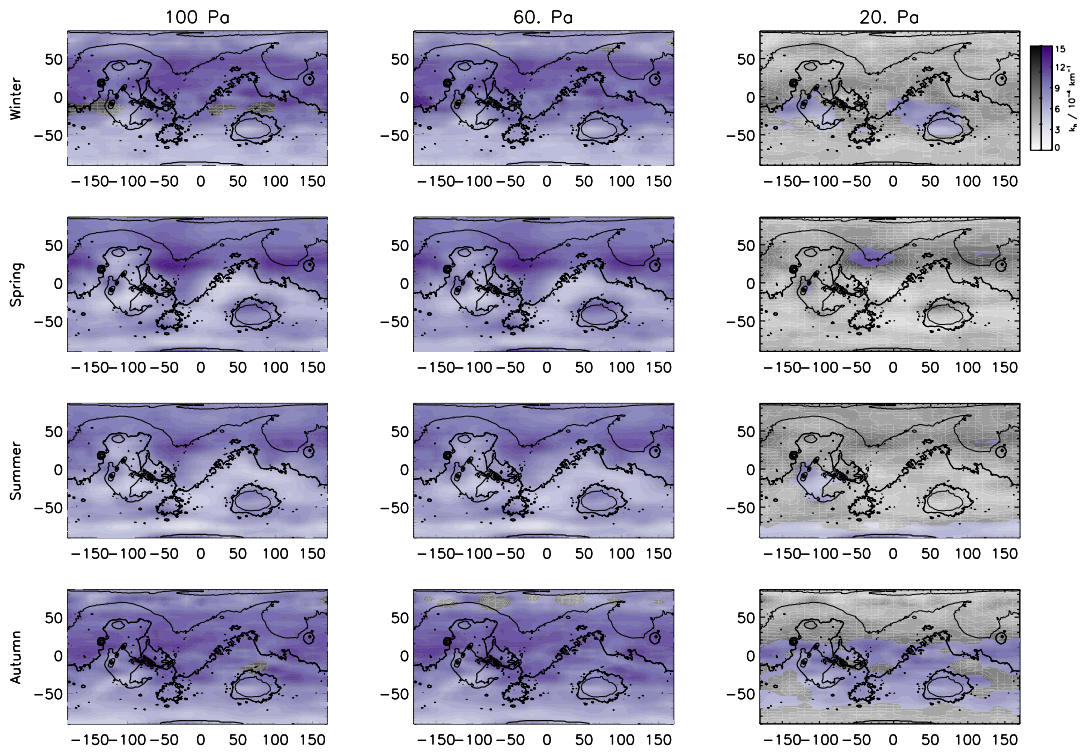


Figure 9: Seasonal mean horizontal wavenumbers, mapped at three heights. Colour bar for all figures at top right.

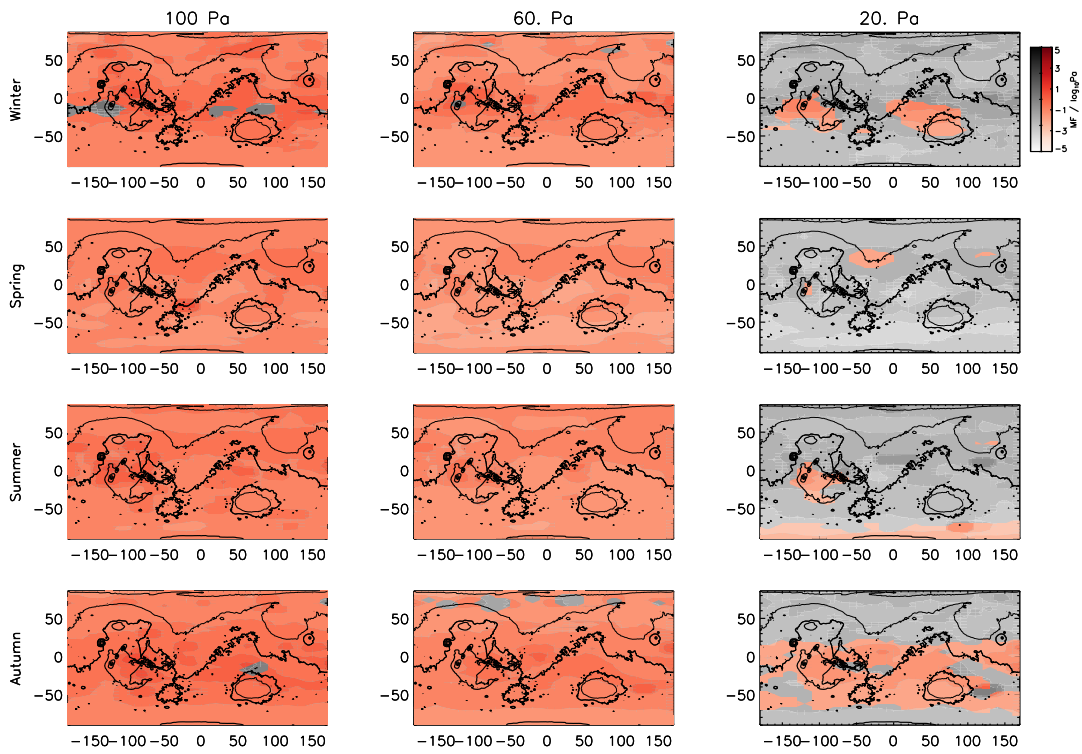


Figure 10: Seasonal mean momentum fluxes, mapped at three heights. Colour bar for all figures at top right.

this, the results observed are somewhat ‘splotchy’, with small localised peaks even in the seasonally-averaged data, consistent with our previous observation that significant quantities of momentum flux appear to be generated by temporally and spatially localised generation are due mechanisms rather than sources which remain consistent throughout the seasons or year. This is particularly the case in the northern hemisphere at the 100 Pa level during winter and, possibly, in the southern hemisphere at the under-resolved 10 Pa level in autumn and winter.

8. Discussion and Conclusions

The values of momentum flux measured demonstrate how important gravity waves driving potentially is to the dynamics of the Martian atmosphere by comparison to Earth. At equivalent altitudes on Earth to the well-sampled portion of the altitude range considered in this study, admittedly under very different dynamical circumstances, typical momentum fluxes measured by the technique used in this paper are $\sim 10^{-5}$ – 10^{-3} Pa [see e.g. figure 3 of Wright and Gille, 2011] as compared to $\sim 10^{-3}$ – 10^{-1} Pa here, a hundredfold difference. Given the significantly lower density of the Martian atmosphere, the effects of this can be expected to be significant.

An important point to note is that the temperature perturbation results obtained are slightly higher than would be expected. We would not expect temperature perturbations to significantly exceed

$$\frac{T'}{T} \sim \frac{N^2 \lambda_z}{2\pi g} \quad (8)$$

which, at the 100 Pa level, would under our assumed values of N and at a typical background temperature of ~ 180 K [Kleinböhl *et al.*, 2009] would support waves of amplitude ~ 11 K. At this altitude, however, we observe temperature perturbations ~ 10 – 18 K. Values may thus be significantly overestimated based on this estimate, which should be borne in mind when considering the results. Possible reasons for this may include insufficiently removed planetary wave/tidal modes in the data, resolution limitations, or limitations in the initial temperature retrieval. Momentum fluxes are directly proportional to temperature perturbations, and consequently would be expected to be overestimated in the same way.

The rough orography of the southern hemisphere would be expected to generate significant mountain wave activity [Collins *et al.*, 1997]. Our results suggest

that this may potentially be the case to some extent. On average, horizontal wavenumbers are higher, and hence wavelengths shorter, in the northern hemisphere, suggesting by analogy with the Earth that a greater proportion of waves in the north are convectively generated [e.g. Alexander *et al.*, 1995, 2002, Alexander and Barnet, 2007] by comparison to the southern. However, any effect this may have on momentum driving of the atmosphere is small: momentum fluxes are not significantly higher in the southern hemisphere than they are in the northern, and while wave amplitudes may rise in the southern hemisphere in autumn and winter (that is to say local summer), their peak amplitudes are little higher than the equivalent values observed in the northern hemisphere in their summer. There also appears to be minimal association between wave features and large-scale topography, with the possible exception of the 100 Pa and 60 Pa temperature perturbations in autumn and winter; however, these larger temperature perturbations do not appear to significantly alter the measured momentum fluxes. Our results hence concur with those of Creasey *et al.* [2006], who observed that wave activity, while slightly correlated with topography in some regions, was not well-predicted by topographic forcing schemes, which fail to produce the substantial tropical forcings observed throughout the year.

9. Acknowledgements

The author would like to thank the MCS team for many years hard work obtaining and producing the data used and David Mulholland and Jo Barstow for useful discussions on the material presented in this article.

The National Center for Atmospheric Research is sponsored by the National Science Foundation. Any opinions, findings and conclusions or recommendations expressed in the publication are those of the author(s) and do not necessarily reflect the views of the National Science Foundation.

References

- Alexander, M. J., and C. Barnet 2007. Using Satellite Observations to Constrain Parameterizations of Gravity Wave Effects for Global Models. *J. Atmos. Sci.* 64(5), 1652–1665.
- Alexander, M. J., J. Gille, C. Cavanaugh, M. Coffey, C. Craig, V. Dean, T. Eden, G. Francis, C. Halvorson, J. Hannigan, R. Khosravi, D. Kinneson, H. Lee, S. Massie, B. Nardi, and A. Lambert 2008. Global estimates of gravity wave momentum flux from High Resolution Dynamics Limb Sounder (HIRDLS) observations. *Journal of Geophysical Research* 113.
- Alexander, M. J., J. R. Holton, and D. R. Durran 1995. The Gravity Wave Response above Deep Convection in a Squall Line Simulation. *J. Atmos. Sci.* 52(12), 2212–2226.

- Alexander, M. J., T. Tsuda, and R. A. Vincent 2002. Latitudinal Variations Observed in Gravity Waves with Short Vertical Wavelengths. *J. Atmos. Sci.* 59(8), 1394–1404.
- Andrews, D. G. 2000. *An Introduction to Atmospheric Physics*. Cambridge University Press.
- Angelats i Coll, M., F. Forget, M. A. López-Valverde, and F. González-Galindo 2005. The first Mars thermospheric general circulation model: The Martian atmosphere from the ground to 240 km. *Geophysical Research Letters* 32(4).
- Barnes, J. R. 1990. Possible Effects of Breaking Gravity Waves on the Circulation of the Middle Atmosphere of Mars. *Journal of Geophysical Research* 95(B2).
- Briggs, G. A., and C. B. Leovy 1974. Mariner Observations of the Mars North Polar Hood. *Bull. Amer. Meteor. Soc.* 55(4), 278–296.
- Collins, M., S. R. Lewis, and P. L. Read 1997. Gravity wave drag in a global circulation model of the Martian atmosphere: Parameterisation and validation. *Advances in Space Research* 19(8), 1245–1254.
- Creasey, J. E., J. M. Forbes, and D. P. Hinson 2006. Global and seasonal distribution of gravity wave activity in Mars' lower atmosphere derived from MGS radio occultation data. *Geophysical Research Letters* 33(1).
- Ern, M., P. Preusse, M. Alexander, and C. D. Warner 2004. Absolute values of gravity wave momentum flux derived from satellite data. *Journal of Geophysical Research* 109.
- Fritts, D. C., and M. J. Alexander 2003. Gravity Wave Dynamics and Effects in the Middle Atmosphere. *Reviews of Geophysics* 41.
- Fritts, D. C., L. Wang, and R. H. Tolson 2006. Mean and gravity wave structures and variability in the Mars upper atmosphere inferred from Mars Global Surveyor and Mars Odyssey aerobraking densities. *Journal of Geophysical Research* 111(A12).
- Imamura, T., and H. Kobayashi 2009. Wavenumber spectra of planetary-scale disturbances in the Mars atmosphere. *Icarus* 199(2), 286–294.
- Joshi, M. M., B. N. Lawrence, and S. R. Lewis 1995. Gravity wave drag in three-dimensional atmospheric models of Mars. *Journal of Geophysical Research* 100(E10).
- Kleinböhl, A., J. T. Schofield, D. M. Kass, W. A. Abdou, C. R. Backus, B. Sen, J. H. Shirley, W. G. Lawson, M. I. Richardson, F. W. Taylor, N. A. Teanby, and D. J. McCleese 2009. Mars Climate Sounder limb profile retrieval of atmospheric temperature, pressure, and dust and water ice opacity. *Journal of Geophysical Research* 114(E10).
- Magalhães, J. A., J. T. Schofield, and A. Seiff 1999. Results of the Mars Pathfinder atmospheric structure investigation. *Journal of Geophysical Research* 104(E4).
- McCleese, D. J., J. T. Schofield, F. W. Taylor, S. B. Calcutt, M. C. Foote, D. M. Kass, C. B. Leovy, D. A. Paige, P. L. Read, and R. W. Zurek 2007. Mars Climate Sounder: An investigation of thermal and water vapor structure, dust and condensate distributions in the atmosphere, and energy balance of the polar regions. *Journal of Geophysical Research* 112.
- Pirraglia, J. A. 1976. Martian atmospheric Lee waves. *Icarus* 27(4), 517–530.
- Stockwell, R. G., and R. P. Lowe 2000. Airglow imaging of gravity waves 1. Results from a small network of OH nightglow scanning imagers. *Journal of Geophysical Research* 106(D15).
- Stockwell, R. G., L. Mansinha, and R. P. Lowe 1996. Localization of the Complex Spectrum: The S Transform. *IEEE Transactions on Signal Processing* 44(4), 998–1001.
- Wang, L., D. C. Fritts, B. P. Williams, R. A. Goldberg, F. J. Schmidlin, and U. Blum 2006. Gravity waves in the middle atmosphere during the macwave winter campaign: evidence of mountain wave critical level encounters. *Annales Geophysicae* 24(4), 1209–1226.
- Wright, C. J., and J. C. Gille 2011. HIRDLS observations of gravity wave momentum fluxes over the monsoon regions. *Journal of Geophysical Research* 116(D12), D12103+.